RSC Advances

PAPER

View Article Online
View Journal | View Issue

Cite this: *RSC Adv.*, 2026, **16**, 1143

A porous flower-like boron and nitrogen co-doped diamond film electrode for the enhanced detection of copper ions

Meixuan Li,[ab] Mingchao Yang,[c] Xiaoxi Yuan, *[a] Chunjiang Li,*[b] Feng Yang*[a] and Dan Yu[b]

Received 10th November 2025
Accepted 13th December 2025

DOI: 10.1039/d5ra08656f

rsc.li/rsc-advances

In this study, a new sensor of porous flower-like boron and nitrogen co-doped diamond (PFBND) was successfully manufactured without using a mask or reactive ion etching. A PFBND electrode was constructed based on the diamond growth mode. PFBND was obtained by removing the non-diamond carbon (NDC) from the PFBND/NDC composite. A PFBND film with a larger surface area and better electrochemical properties was obtained. The PFBND sensor exhibited significant advantages for detecting trace Cu^{2+} using differential pulse anodic stripping voltammetry. The finite element numerical method was used to get the electrolyte current intensity vector near the PFBND tip. The limit of detection was low at 0.28 μg L^{-1}, and a broad linear range of 1–100 μg L^{-1} was achieved. The sensor exhibited excellent selectivity for detecting copper ions against common interfering ions, ensuring reliable detection in complex environmental samples. Its practical applicability was validated through recovery tests.

1. Introduction

With the development of industries and agriculture, heavy metal pollution has emerged as a serious worldwide environmental issue.[1–3] Cu^{2+} (copper ion), being among the most toxic and widely distributed heavy metal ions, is distributed extensively and has a high content in many environmental systems.[4,5] Exposure to Cu^{2+} in the environment can pose a serious risk of cancer and lead to organ damage, including kidney dysfunction, high blood pressure, teratogenic effects, impairment of the immune system, and bone-related disorders.[6] According to the standards of the World Health Organization, the maximum permissible concentration of Cu^{2+} in drinking water is 1 mg L^{-1}.[7,8] Due to the long half-life and non-biodegradability of Cu^{2+}, once it enters the human body, even at low concentration levels, it will continue to accumulate and cause significant harm to the human health.[9,10] Therefore, the establishment of efficient and sensitive Cu^{2+} detection methods is of great significance.

At present, traditional analytical techniques for monitoring Cu^{2+} include inductively coupled plasma mass spectrometry, high-performance liquid chromatography, ultraviolet visible spectroscopy and X-ray fluorescence spectroscopy.[11–13] Although these detection technologies have the advantages of high resolution and accuracy, they are limited by the use of large instruments, cumbersome pre-processing, and high costs, making it difficult to meet the real-time screening needs in the field.[14–16] Therefore, the establishment of an efficient, easy-to-operate, and reliable electrochemical detection method for Cu^{2+} has become an urgent necessity.[17–19]

Electrochemical detection has become the preferred method for Cu^{2+} analysis due to its accuracy, speed, affordability, sensitivity, ability to simultaneously determine multiple components, and suitability for on-site operations.[20] Nanomaterials have become important candidates for improving electrode performance due to their large specific surface area and easy modification properties.[21–24] Through nanoscale surface design, catalytic activity, conductivity, effective reaction area, and charge transfer rate can be simultaneously improved, and signals can be further amplified by leveraging size effects and functionalization advantages.[25] Nanostructured diamond electrodes have become an ideal choice for the electrochemical detection of trace Cu^{2+} due to their wide potential window, low background current, extremely high stability, strong anti-pollution ability, high sensitivity, excellent reproducibility and environmental friendliness.[26] In contrast, other carbon nanomaterials usually have shortcomings in these key properties, especially in terms of long-term stability, anti-pollution ability and wide potential window. Therefore, in situations where high sensitivity, high stability and green detection are required,

[a]*Institute for Interdisciplinary Quantum Information Technology, Educational Robot Research Center, Jilin Engineering Normal University, Changchun 130052, PR China. E-mail: limx@jlenu.edu.cn; xxyuan@jlenu.edu.cn; yangfeng@jlenu.edu.cn*

[b]*Changchun City GangHeng Electronics Co., Ltd, China, Changchun 130000, PR China. E-mail: ccsghdz@163.com; CJLIgangheng@163.com*

[c]*College of Physical Science and Technology, Hebei Normal University of Science and Technology, Qinhuangdao 066004, PR China*

nanostructured diamond electrodes are a better choice.[27] Among various types of nano-modified layers, boron-doped diamond and its derivative systems stand out for their high conductivity, biocompatibility, low noise, and corrosion resistance.[28,29] If nitrogen, sulfur, and other heteroatoms are co-doped, the electrocatalytic activity might be enhanced, for the larger the specific surface area, the denser the active sites and the higher the sensitivity of electroanalysis. Therefore, nanostructured doped diamond is considered the core direction of the next-generation sensing platform.

The traditional "top-down" preparation of nanodiamond electrodes (plasma/catalysis/thermal etching, *etc.*) relies on masks and subsequent removal steps, which are cumbersome and costly, making it difficult to scale up applications. The aim of this study is to use porous flower-like boron and nitrogen co-doped diamond sensor (PFBND) electrodes for electrochemical detection of Cu^{2+}, without the need for etching masks. PFBND can be prepared by removing non-diamond carbon (NDC) present in PFBND/NDC composites. The traditional top-down preparation method requires growing a certain thickness of diamond and then etching the upper layer of diamond to form nanostructured diamond. The porous flower-like diamond prepared by the bottom-up method in this study utilizes the growth orientation of diamond. During the growth period, both diamond and non-diamond carbon (NDC) mixed phases are grown simultaneously, and then, NDC is removed by annealing. The process of etching NDC saves a significant amount of cost and time compared to etching diamond. Compared with the conventional top-down nanodiamond fabrication approaches, this work employs a growth-regulated, post-annealing strategy to create porous flower-like diamond without masks or reactive ion etching, offering advantages in cost, simplicity, and scalability, which is conducive to industrial applications.

Among various electrochemical detection techniques, differential pulse anodic stripping voltammetry (DPASV) is generally regarded as the "golden method" for *in situ* determination of trace Cu^{2+} due to its high sensitivity, fast analysis speed, and portable instrument.[30,31] The experimental results confirm that the combination of the PFBND electrode exhibits excellent detection performance for Cu^{2+}.

This study also introduces finite element simulation to explore the application prospects of the "tip current collection" effect in enhancing current density. The PFBND electrode has demonstrated multiple leading performance indicators in the detection of trace Cu^{2+}, with a linear detection range of 1–100 μg L^{-1}, providing a scalable next-generation sensing platform for *in situ* monitoring of heavy metal ions.

2. Materials and methods

2.1. Materials

$Cu(NO_3)_2$ (99.9%, guaranteed reagent grade) was purchased from Sigma-Aldrich. A 0.1 M acetate buffer solution composed of sodium acetate and glacial acetic acid was used. Remaining reagents, including potassium ferricyanide (II), potassium ferrocyanide trihydrate (III), and KCl, were of analytical grade and were used without further purification. All experimental procedures used 18.2 MΩ cm ultra-pure water.

2.2. Preparation of the PFBND electrode

Boron and nitrogen co-doped diamond films were deposited onto P-type Si substrates using a microwave plasma CVD system by employing a microwave frequency of 2.45 GHz. Mirror-polished P-type Si substrates were immersed in an aqueous solution containing approximately 5 nm nanodiamond powder, and subjected to ultrasonic treatment for 60 minutes. For nucleation site preparation, all substrates were cleaned in ultrasonic cleaning tanks for 10 minutes, successively using acetone, followed by ethanol, and finally deionized water. The substrate was then moved to an N_2 dryer. Reaction gases contained CH_4 and H_2, and the boron source was $B(OCH_3)_3$ (liquid), using an H_2 gas flow. Firstly, the $CH_4/H_2/B/N_2$ flow values were set at (20/200/2/1 sccm) to form the PFBND/NDC composite for 6 hours. NDC was removed by annealing the composite at 800 °C in air for 20 minutes.

2.3. Apparatus

The surface morphology of the PFBND film was observed using a scanning electron microscope (SEM, model JSM-6480LV). Carbon phase analysis was performed using a Renishaw inVia Raman microscope with a laser wavelength of 532 nm. The chemical bonds on the surface and the chemical states of the surface were obtained by X-ray photoelectron spectroscopy (XPS, VG ESCALAB MK II). All the electrochemical characterization was performed with the CHI 760E Electrochemical Workstation.

2.4. Electrochemical measurements

In the three-electrode system, a platinum wire was used as the counter electrode, a saturated calomel electrode as the reference electrode, and the PFBND film as the working electrode with an area of 0.10 cm^2. Electrochemical impedance spectroscopy (EIS) measurements were conducted in a solution containing 5 mM $[(CN)_6]^{3-/4-}$ and 0.1 M KCl. Cyclic voltammetry (CV) and DPASV were employed to characterize the electrochemical performance of PFBND electrodes in 0.1 M acetate buffer (pH = 5.5) at 30 °C. The electrochemical measurements were repeated at three times, and the electrochemical data are presented as mean ± standard deviation. The limit of detection (LOD) was calculated as $3\sigma/S$, where σ is the standard deviation of the blank signal (zero-concentration response) and S is the slope of the calibration curve. The linear range (1–100 μg L^{-1}) was determined from the DPASV response. Sensitivity corresponds to the slope of the calibration plot.

2.5. COMSOL multiphysics simulations

COMSOL Multiphysics was used to model the free-electron density distribution near the PFBND electrodes, and the "Electric Currents" module was used to calculate the number of free electrons at given potentials. The intensity of the electric field

(E) was calculated from the formula $E = -\nabla V$, representing the negative gradient of potential V. The electrical conductivity of the PFBND electrode was set to 2×10^4 S m^{-1}, while current density (ρ) was derived from Gauss's law of electric fields with $\rho = \varepsilon_r\varepsilon_0\nabla\cdot E$, where E denotes electric field intensity, ε_0 is the vacuum permittivity, and ε_r represents the material's dielectric constant.

3. Results and discussion

3.1. Morphology and structure of the PFBND films

During diamond growth, hydrogen plasma cannot remove all NDC; there will be some residual NDC left on the wafer, as CH_4 alone takes up such an enormous percentage. Fig. 1 exhibits SEM images of the PFBND/NDC composite and PFBND film. From Fig. 1a, we can find that there is some black material, which might being NDC residue on the surface of the diamond. At the same time, nitrogen is added for nucleation of diamonds; thus, the surface of PFBND/NDC composite becomes granular. The PFBND/NDC composite material was annealed in air at 800 °C for 20 minutes to remove the NDC phase, resulting in PFBND films, as shown in Fig. 1b. The annealing process (800 °C in air) primarily removes the NDC phase *via* oxidation, as NDC oxidizes more readily than diamond. This selectively etches away the surrounding NDC matrix, thereby exposing and sharpening the underlying porous flower-like diamond structures that were already formed during growth. The process is thus mainly a selective removal rather than a surface reconstruction of diamond. According to Fig. 1c, the PFBND/NDC composite has a grain size range of 200–300 nm; at higher magnifications captured by high-magnification SEM imaging (Fig. 1d), it shows a vertically aligned nanostructure created by nitrogen incorporation, exhibiting columnar growth patterns and having tip dimensions in the nanoscale range. Compared with the conventional layer-structured method of PFBND fabrication, the current method features an easier fabrication process, better cost, and faster processing speed due to controllable synthesis without the need for templates or specialized higher-cost etching devices.

The OES results of the growth stage of the PFBND/NDC composite films are given in Fig. 2. Emission lines of atomic hydrogen (H_α, 656 nm; H_β, 486 nm), molecular hydrogen (H_2, 580 nm), and carbonaceous CN (386 nm) and CH_4 (432 nm and 766 nm), and C_2 (516 nm) bands are observed. Higher CH_4 concentrations lead to more intense carbonaceous C_2 bands, indicating that there is an excessive amount of secondary nucleation of C_2 (too many seeds), which inhibits the formation of a good quality diamond crystal and creates more NDC. This results in a diamond and NDC composite structure. CN species have two functions, they make it possible to create nanocolumns and are secondary nucleation sites during the competition between diamond and NDC, confining diamond grain growth to allow for nanoscale growth. The porous flower-like structure formation is attributed to the synergistic effect of N and B. N-doping is conducive to the formation of (100) crystal plane in diamond. The growth of (100) crystal plane is not a simple vertical growth but a rotational growth. The addition of B is beneficial for increasing the growth rate of diamond, resulting in rapid helical growth of (100) plane and a porous structure on the radial side, which leads to the porous flower-like morphology. Then, removing NDC from the composite yields the PFBND film.

A comparison of the Raman spectra of the PFBND/NDC composite film and the annealed PFBND film is shown in Fig. 3. The low quality of the PFBND/NDC composite film is consistent with the Raman spectrum (blue line in Fig. 3), where the wide band around 1550 cm^{-1} corresponds to NDC, which results from a high concentration of CH_4 during the growth of diamond, and the typical diamond peak located at 1332 cm^{-1} is weakened. The peaks at 500 cm^{-1} and 1200 cm^{-1} are due to the Fano effect from heavy boron doping. The annealing of the composite at 800 °C for 20 minutes will cause NDC to go away, leaving PFBND film behind. The annealed PFBND gives a clear diamond peak at 1332 cm^{-1} and also shows a reduced NDC

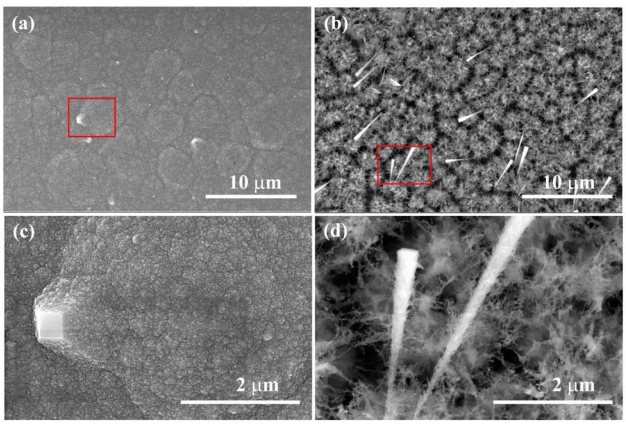

Fig. 1 SEM images of the (a) PFBND/NDC composite film deposited by $CH_4/H_2/B/N_2$ gas flow rates of 20/200/2/1 sccm and (b) PFBND film obtained by annealing the above composite film in air at 800 °C for 20 min to remove NDC. (c) and (d) Enlarged images of (a) and (b), respectively.

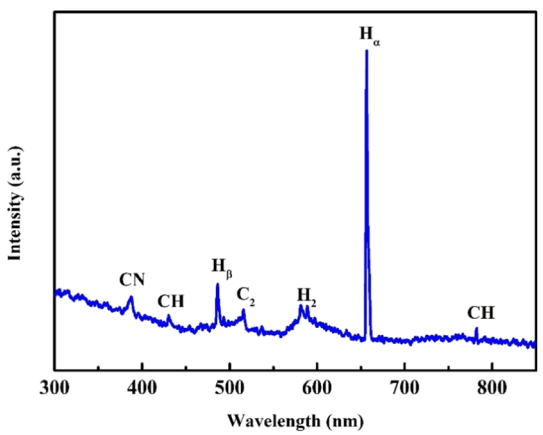

Fig. 2 Optical emission spectroscopy (OES) results obtained during the growth phase of the PFBND/NDC composite film.

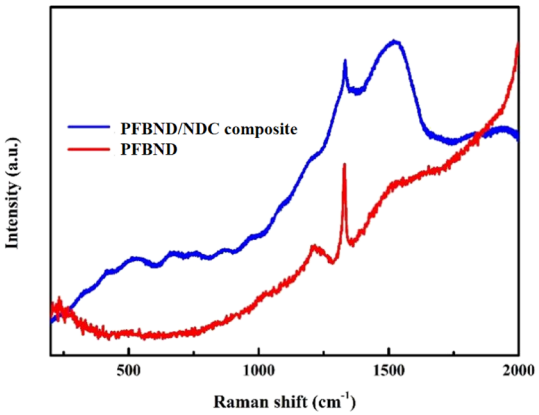

Fig. 3 Comparison of the Raman spectra of the PFBND/NDC composite film (blue line) and annealed PFBND film (red line).

peak with a center frequency at 1550 cm^{-1}, which is indicated by the red line in Fig. 3.

The elemental composition of PFBND was measured by XPS. B (3.01%), C (92.42%), N (3.28%), and O (1.28%) were identified in the XPS high-resolution spectra of PFBND (Fig. 4). The B 1s (191.7 eV), C 1s (284.6 eV), N 1s (399.6 eV), O 1s (532.8 eV) peaks correspond to co-doping.[32] High resolution scans (Fig. 4a–d) showed that B 1s is split into B–C (191.5 eV), C 1s is deconvolved into sp^2 C–C (284.1 eV) and sp^3 C–C (284.5 eV) and C–O (286.3 eV), and N 1s is fitted into C–N–C (399.4 eV) and C–N (400.2 eV), while O 1s is deconvoluted into C–O (532.9 eV).[33–35] Air annealing causes surface oxidation, generating carbon–oxygen associations vital for electrochemical activity.[36,37]

3.2. Electrochemical performance of PFBND electrode

Fig. 5a shows the CV test results of the PFBND/NDC composite and the PFBND electrode. PFBND exhibits 8.5 times more surface area than the PFBND/NDC electrode, with more active sites for the electrochemical detection. The EIS measurements, seen in Fig. 5b, show that the PFBND electrode has a faster charge transfer resistance than the composite. This is consistent with the enhanced charge transfer kinetics at the electrode–electrolyte interface. The Fig. 5b shows a smaller charge transfer resistance in the EIS spectrum of PFBND,[38] as corroborated by the SEM image of the porous flower-like nanostructure.[39] The low-frequency semicircle is attributed to the Faraday reaction charge transfer resistance. These results reveal that PFBND, with its larger surface area and improved charge

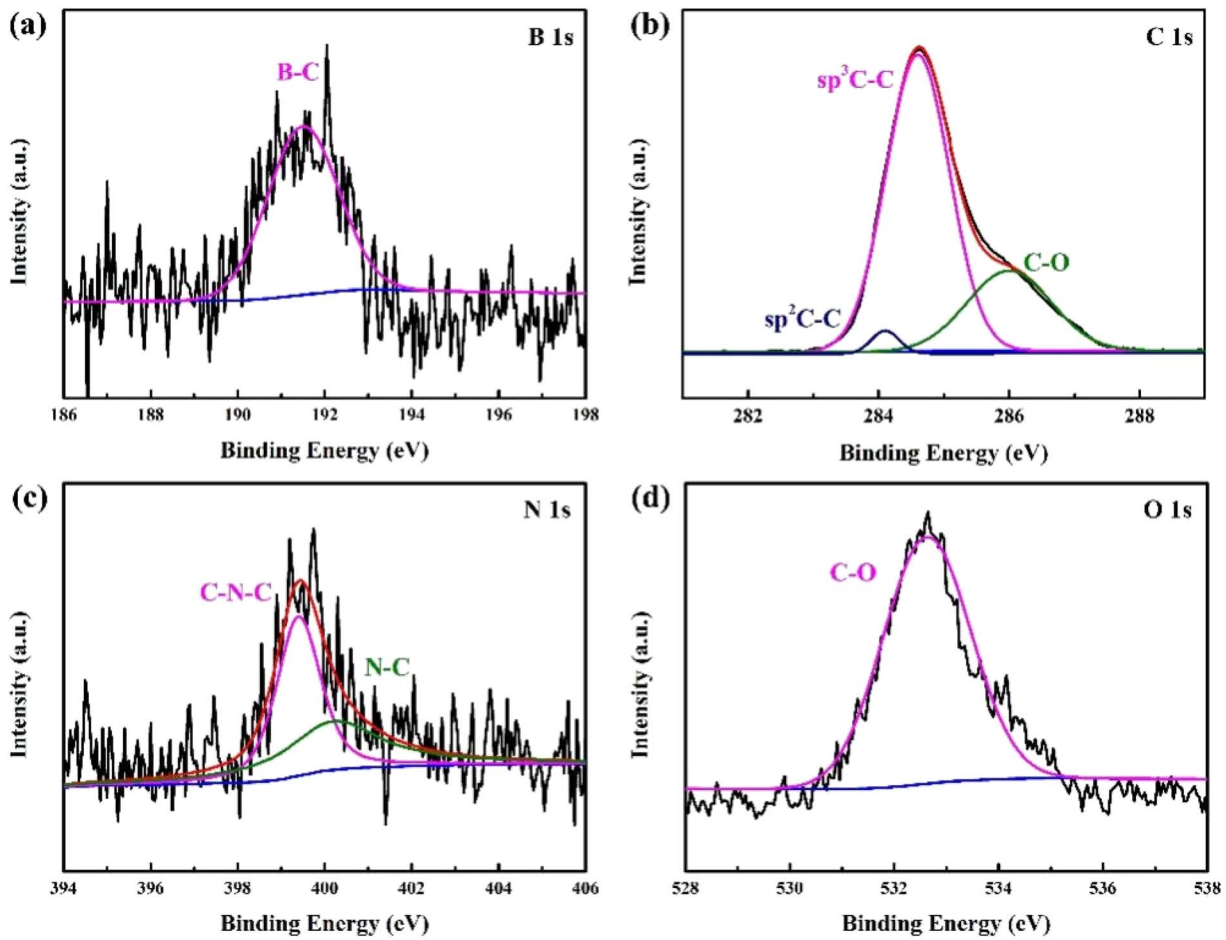

Fig. 4 XPS high-resolution spectra of PFBND: B 1s (a), C 1s (b), N 1s (c), and O 1s (d).

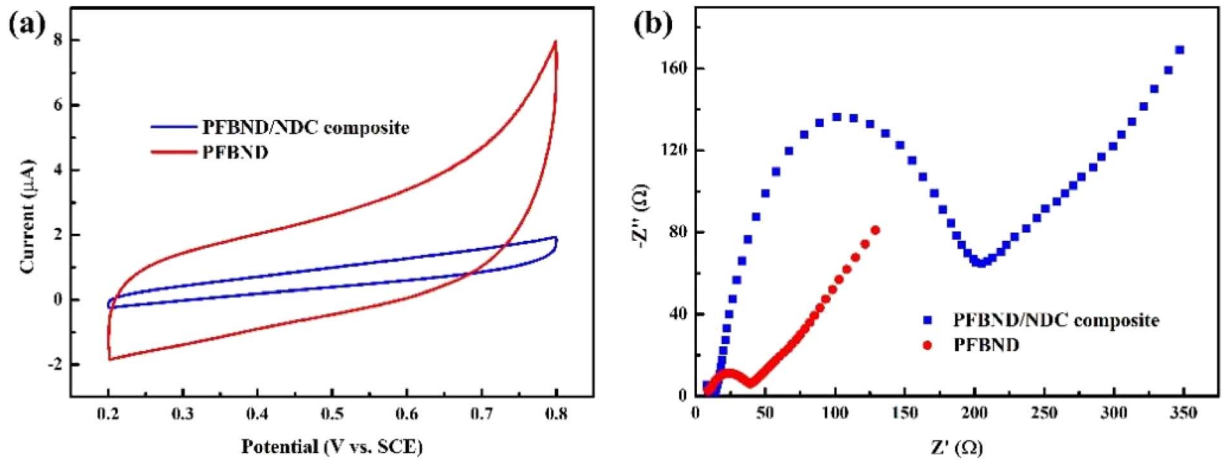

Fig. 5 (a) CV curves of the PFBND/NDC composite and PFBND in 0.1 M acetate buffer (scan rate = 50 mV s^{-1}). (b) EIS of the PFBND/NDC composite and PFBND in 5 mM Fe $(CN)_6^{3-/4-}$ solution with 0.1 M KCl.

transfer, enables significantly better electrochemical sensing performance.

3.3. Electrochemical sensing performance for detecting Cu^{2+}

To optimize the Cu^{2+} detection conditions, DPASV analysis was conducted with the PFBND electrode under pre-accumulation conditions of pH = 5.5, −1.0 V deposition potential, and 270 s deposition time. Fig. 6a shows the DPASV of different concentrations of Cu^{2+} with ranges of 1–100 μg L^{-1}. In this range, the stripping peak potential moves slightly toward the positive direction, while the concentration of Cu^{2+} is increased and reaches as high as −0.758 V, −0.751 V, −0.747 V, and −0.741 V when the concentrations are 40, 60, 80, and 100 μg per L Cu^{2+}, respectively. This is also consistent with a previous study reporting that the increase in Mn^{+}/M equilibrium reduction voltage and the presence of more Mn metal particles on the electrocatalyst surface lead to increased peak voltages.[40,41] The heterogeneity of the PFBND electrode, characterized by varying grain structures, electrical conductivities, and surface morphologies, results in varied peak positions.

The calibration plot shown in Fig. 6b is linear with good correlation coefficients. The sensitivity is within the range from 1 to 100 mg L^{-1} for Cu^{2+}. Based on the response of three times the standard deviation of zero-potential response, the LOD value is 0.28 μg L^{-1}, which shows that the PFBND films can be used for the analysis of trace amounts of Cu^{2+}. In comparison with previously reported diamond-based Cu^{2+} sensors (Table 1),[42–45] the advantage of the PFBND electrode is evident: it has a good linear range and a lower LOD.

3.4. Simulations of current density near the PFBND tip

To study the mechanism of how Cu^{2+} is stripped away from the electrode, COMSOL Multiphysics software can be used for current density distribution simulation around the PFBND

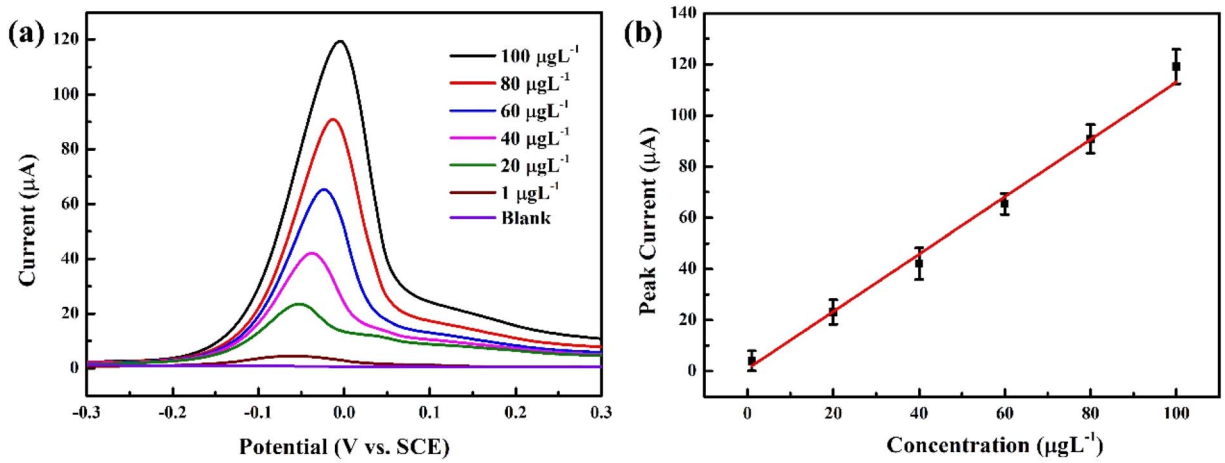

Fig. 6 (a) DPASV responses of the PFBND electrode during the detection of Cu^{2+} solutions (1–100 μg L^{-1}). The DPASV curve shown represents the average of three repeated measurements. (b) Calibration curve for Cu^{2+} detection; the error bars represent the relative standard deviation (RSD) of three determinations. Experimental conditions: 0.1 M acetate buffer (pH = 5.5).

Table 1 Diamond electrodes reported in the literature for detecting Cu^{2+a}

Electrodes	Technique	Medium	Linear range ($\mu g\ L^{-1}$)	LOD ($\mu g\ L^{-1}$)	Ref.
Flat BDD	SWASV	0.1 M HCl pH = 1.0	2–40	1.42	42
Carbide/BDD	DPASV	0.1 M acetate buffer pH = 5.0	1–1000	0.74	43
Graphite/diamond	DPASV	0.1 M acetate buffer pH = 5.0	5–1000	0.47	44
BDD/Ti	DPASV	0.25 M KCl and 0.25 M KNO_3 pH = 1.65	5.1–100	5.1	45
PFBND	DPASV	0.1 M acetate buffer pH = 5.5	1–100	0.28	This work

[a] BDD: boron-doped diamond; SWASV: square wave anodic stripping voltammetry.

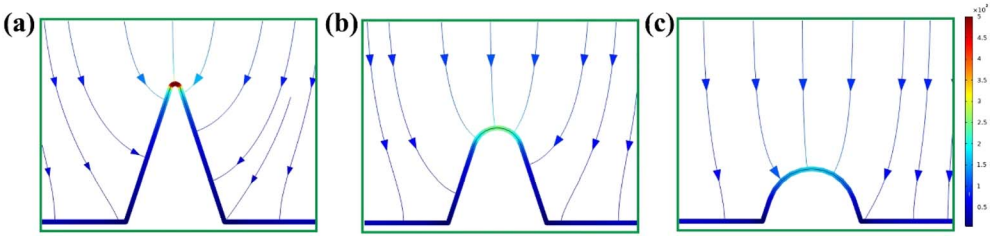

Fig. 7 Current density distribution on the surface of the PFBND tip with the tip radius being (a) 10 nm, (b) 50 nm, and (c) 90 nm.

electrode. With respect to the quantitative and qualitative changes in current density, attention was concentrated on the output of the electrode–electrolyte interface. The rounded-tip cone models were used to construct nanoscale tips of PFBND in an electrolyte environment (Fig. 7). We analyzed the current density distribution for the tip radii of 10 nm, 50 nm, and 90 nm, with the maximum value being 6.67×10^2 A m^{-2} for 10 nm (Fig. 7a), 2.21×10^2 A m^{-2} for 50 nm (Fig. 7b), and 1.42×10^2 A m^{-2} for 90 nm (Fig. 7c). The tip with a 90 nm radius transitions to that of 10 nm radius, resulting in a 4.7-fold increase of current density. As can be observed, the local current density indeed becomes higher when curvature geometries are employed. It could help Cu^{2+} concentration enrichment at the PFBND tips to enhance synergistic deposition for low-concentration Cu^{2+} with DPASV.

Reproducibility was assessed by calculating the RSD of stripping peak currents when 6 repetitive tests of 100 μg per L Cu^{2+} were performed using the PFBND electrode. After each measurement, a constant potential of +0.5 V was applied for 600 s to wash the deposits off the electrode surface. Even though the PFBND electrode detected Cu^{2+} multiple times, there was no change in stripping peak potential, but there was a decrease in the stripping peak current intensity. The calculated RSD value of 3.1% indicates that the PFBND electrode has good reproducible accuracy.

A selectivity experiment was carried out to study the anti-interference capability in the presence of interfering ions Pb^{2+}, Zn^{2+}, Ca^{2+}, Cu^{2+}, Mg^{2+}, and Na^{+}, which were introduced at 10 times the concentration of Cu^{2+}. From Fig. 8, the little change in the signal when adding these interfering ions to Cu^{2+} demonstrates that the PFBND electrode has a strong resistance to the tested cations. The introduction of nitrogen forms a small amount of sp^2 graphite phase in diamond, which works in synergy with the hole conduction generated by boron doping, jointly enhancing the charge transfer efficiency and reducing the internal resistance of the electrode. The tip curvature effect of nanostructures is crucial for efficient reduction deposition. The nanoflower-like and porous structure formed by co-doping induction greatly increases the effective surface area of the electrode, providing more active sites for the deposition of heavy metal ions and thereby enhancing the dissolution signal. Therefore, this electrode has an excellent effect in detecting heavy metal copper ions.

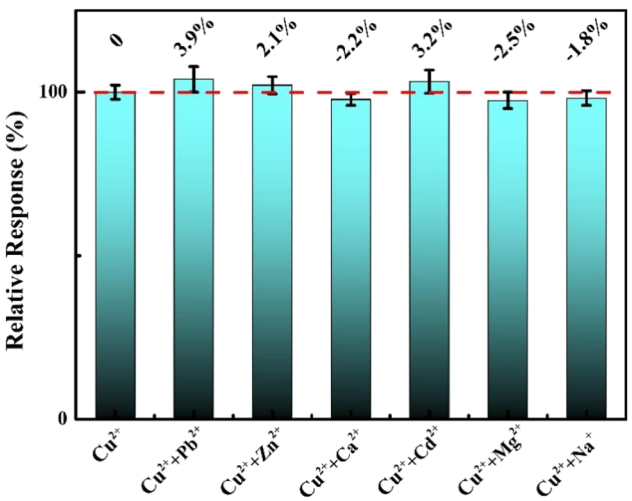

Fig. 8 Bar graph showing the selective ability of the PFBND electrode to resist ion interference.

4. Conclusions

In this work, we successfully synthesized PFBND films from H_2/CH_4/B/N_2 gas mixtures followed by air annealing, without masks or reactive ion etching. By using the co-doped diamond growth method and eliminating NDC in the PFBND/NDC composite, the PFBND electrode exhibited a larger surface area. Electrochemical sensing experiments showed that the detection of Cu^{2+} has a good linearity in the range of 1–100 μg L^{-1} with a low LOD of 0.28 μg L^{-1}. The larger specific surface area of PFBND improved the electrochemically active sites. The sharp tip enhancing current density might increase local Cu^{2+} concentration near the PFBND electrode. This kind of structural advantage would cause local concentration enrichment of Cu^{2+} near the surface of PFBND. Thus, the sensor was sensitive and reliable in the Cu^{2+} detection. The results indicated that the PFBND electrodes had potential as good candidates for the real-time determination of heavy metal ions in environmental samples. However, a current limitation is that the long-term stability of the sensor in extreme pH requires further investigation. We would focus on enhancing the stability of heavy metal ion detection for field testing in extreme pH, and on exploring its applicability for simultaneous on-site detection of multiple heavy metals in future work.

Author contributions

Conceptualization, M. L.; methodology, X. Y.; software, F. Y.; formal analysis, C. L.; investigation, D. Y.; data curation, X. Y.; writing—original draft preparation, M. L.; writing—review and editing (equal); project administration, X. Y. All authors have read and agreed to the published version of the manuscript.

Conflicts of interest

The authors declare no conflict of interest.

Data availability

The data generated or analyzed during the current study are available from the corresponding authors (Xiaoxi Yuan, Chunjiang Li, and Feng Yang) upon reasonable request. All relevant experimental procedures, characterization methods (including SEM, Raman spectroscopy, XPS, and electrochemical measurements), and simulation parameters are described in detail within the manuscript to ensure the reproducibility of the work. The raw data supporting the conclusions of this study have not been made publicly available due to ongoing related research but will be shared by the authors without undue reservation.

Acknowledgements

This work was funded by the Science and Technology Planning Project of Jilin Province No. 20250602009RC. We acknowledge the support of the State Key Lab of Superhard Materials, Jilin University, Changchun 130012, PR China.

References

1 J. Gao, J. Yin, G. Wang, X. Wang, J. Zhang, B. Sun, D. He, H. Suo and C. Zhao, *Food Chem.*, 2024, **448**, 138994.
2 Y. Zhang, K. Xu, L. Van Tan, H. Tan and H. Zhang, *Microchim. Acta*, 2024, **191**, 246.
3 M. Li, Q. Shi, N. Song, Y. Xiao, L. Wang, Z. Chen and T. D. James, *Chem. Soc. Rev.*, 2023, **52**, 5827–5860.
4 H. Sohrabi, A. Khataee, S. Ghasemzadeh, M. R. Majidi and Y. Orooji, *Trends Environ. Anal. Chem.*, 2021, **31**, e00139.
5 M. Yence, A. Cetinkaya, G. Ozcelikay, S. I. Kaya and S. A. Ozkan, *Crit. Rev. Anal. Chem.*, 2022, **52**, 1122–1138.
6 A. M. Musa, J. Kiely, R. Luxton and K. C. Honeychurch, *TrAC, Trends Anal. Chem.*, 2021, **139**, 116254.
7 A. Plucinski, Z. Lyu and B. V. Schmidt, *J. Mater. Chem. B*, 2021, **9**, 7030–7062.
8 L. Bouida, M. Rafatullah, A. Kerrouche, M. Qutob, A. M. Alosaimi, H. S. Alorfi and M. A. Hussein, *Water*, 2022, **14**, 3432.
9 A. Popenda, E. Wiśniowska and C. Manuel, *Desalination Water Treat.*, 2024, **319**, 100456.
10 M. Shellaiah and K. W. Sun, *Nanomaterials*, 2021, **12**, 64.
11 A. A. Krata, M. Wojciechowski, M. Kalabun and E. Bulska, *Microchem. J.*, 2018, **142**, 36–42.
12 J. Q. Jiang, Y. M. Zhang, T. B. Wei, H. Yao and Q. Lin, *Appl. Organomet. Chem.*, 2022, **36**, e6705.
13 M. Safari, Y. Yamini, M. Y. Masoomi, A. Morsali and A. Mani-Varnosfaderani, *Microchim. Acta*, 2017, **184**, 1555–1564.
14 X. Yuan, M. Yang, X. Wang, Y. Zhu and F. Yang, *Materials*, 2023, **16**, 6986.
15 X. Yuan, Y. Liang, M. Yang, S. Cheng, N. Gao, Y. Zhu and H. Li, *Nanomaterials*, 2023, **13**, 2955.
16 Y. Liang, L. Wan, N. Gao, H. Li and X. Yuan, *Microchem. J.*, 2024, **207**, 111861.
17 S. I. Mohammad, A. Vasudevan, I. Sapaev, M. K. Abosaoda, C.-Y. Hsu, M. Akkur, A. K. Mishra, G. Kaur, R. Singh and A. Mohebi, *RSC Adv.*, 2025, **15**, 40338–40367.
18 W. Yi, Z. He, J. Fei and X. He, *RSC Adv.*, 2019, **9**, 17325–17334.
19 S. S. Nadumane, R. Biswas and N. Mazumder, *RSC Adv.*, 2025, **15**, 11573–11579.
20 G. Aragay, J. Pons and A. Merkoçi, *Chem. Rev.*, 2011, **111**, 3433–3458.
21 J. Xu, N. Yang, S. Heuser, S. Yu, A. Schulte, H. Schönherr and X. Jiang, *Adv. Energy Mater.*, 2019, **9**, 1803623.
22 J. A. Buledi, S. Amin, S. I. Haider, M. I. Bhanger and A. R. Solangi, *Environ. Sci. Pollut. Res.*, 2021, **28**, 58994–59002.
23 H. Li, N. Li, P. Zuo, S. Qu, F. Qin and W. Shen, *J. Colloid Interface Sci.*, 2023, **640**, 391–404.
24 H. Imanzadeh, Y. Sefid-Sefidehkhan, H. Afshary, A. Afruz and M. Amiri, *J. Pharm. Biomed. Anal.*, 2023, **230**, 115390.
25 S. Kempahanumakkagari, A. Deep, K.-H. Kim, S. K. Kailasa and H.-O. Yoon, *Biosens. Bioelectron.*, 2017, **95**, 106–116.
26 S. Mandal, *RSC Adv.*, 2021, **11**, 10159–10182.
27 H. Zhuang, N. Yang, H. Fu, L. Zhang, C. Wang, N. Huang and X. Jiang, *ACS Appl. Mater. Interfaces*, 2015, **7**, 5384–5390.

28 L. Wan, Y. Liang, Y. Yang, Q. Zhang, Z. Cui, J. Liu, S. Cheng, N. Gao, H. Li and X. Yuan, *Diamond Relat. Mater.*, 2024, **144**, 110965.
29 X. Duan, X. Liu, C. Wang, J. Xiang and H. Long, *Diamond Relat. Mater.*, 2024, **147**, 111363.
30 T. Copeland and R. Skogerboe, *Anal. Chem.*, 1974, **46**, 1257A–1268a.
31 W. Zhong, J. Zou, Q. Yu, Y. Gao, F. Qu, S. Liu, H. Zhou and L. Lu, *Food Chem.*, 2023, **402**, 134379.
32 S. Li, B. Zeng, Z. Feng, Y. Liu, W. Yang and L. Zhang, *Thin Solid Films*, 2010, **519**, 251–258.
33 S. Ferro, M. Dal Colle and A. De Battisti, *Carbon*, 2005, **43**, 1191–1203.
34 R. F. Brocenschi, P. Hammer, C. Deslouis and R. C. Rocha-Filho, *Anal. Chem.*, 2016, **88**, 5363–5368.
35 H. Girard, N. Simon, D. Ballutaud, M. Herlem and A. Etcheberry, *Diam. Relat. Mater.*, 2007, **16**, 316–325.
36 J. Zhang, D. S. Su, R. Blume, R. Schlögl, R. Wang, X. Yang and A. Gajović, *Angew. Chem.*, 2010, **122**, 8822–8826.
37 P. M. Dietrich, S. Glamsch, C. Ehlert, A. Lippitz, N. Kulak and W. E. Unger, *Appl. Surf. Sci.*, 2016, **363**, 406–411.
38 S. Kamatchi Jothiramalingam, M. Ficek, K. Panda, C.-J. Yeh, M. Sawczak, J. Ryl, K.-C. Leou, J. Y. Park, I.-N. Lin and R. Bogdanowicz, *ACS Appl. Mater. Interfaces*, 2019, **11**, 48612–48623.
39 X. Yuan, N. Gao, X. Gao, D. Qiu, R. Xu, Z. Sun, Z. Jiang, J. Liu and H. Li, *Sens. Actuators, B*, 2019, **281**, 830–836.
40 H. Zhuang, C. Wang, N. Huang and X. Jiang, *Electrochem. Commun.*, 2014, **41**, 5–7.
41 L. A. Hutton, M. E. Newton, P. R. Unwin and J. V. Macpherson, *Anal. Chem.*, 2011, **83**, 735–745.
42 R. Ferreira, J. Chaar, M. Baldan and N. Braga, *Fuel*, 2021, **291**, 120104.
43 S. Kim, Y. Jeong, M.-O. Park, Y. Jang, J.-S. Bae, K.-S. Hong, S. Kim, P. Song and J.-H. Yoon, *J. Mater. Res. Technol.*, 2023, **23**, 1375–1385.
44 Z. Zhai, N. Huang, H. Zhuang, L. Liu, B. Yang, C. Wang, Z. Gai, F. Guo, Z. Li and X. Jiang, *Appl. Surf. Sci.*, 2018, **457**, 1192–1201.
45 B. Zhao, J. Li, X. Yu, J. Zhang and Y. Ren, *Surf. Rev. Lett.*, 2019, **26**, 1850179.